Impact performance deterioration of stainless steel-LHDCC composite beams under continuous impacts

Xiaolong Zhao[1], Zhenyu Huang[2*], Wei Zhang[3] , Jianqiao Ye[4]

1 Research Assistant. Guangdong Provincial Key Laboratory of Durability for Marine Civil Engineering, Shenzhen University, Shenzhen, China 518060. Email: 347479165@qq.com

2 Associate Professor. Guangdong Provincial Key Laboratory of Durability for Marine Civil Engineering, Shenzhen University, Shenzhen, China 518060. Key Laboratory of Coastal Urban Resilient Infrastructures (MOE), Shenzhen University, Shenzhen, China 518060. Email: huangzhenyu@szu.edu.cn

3 Research Associate. Shenzhen Urban Public Safety and Technology Institute, Shenzhen, China 518046. Email: zhangwdnv@gmail.com

4 Professor. Department of Engineering, Lancaster University, Lancaster LA1 4YR, UK. Email: j.ye2@lancaster.ac.uk

Abstract

Engineering structures serving in the marine environment may be subjected to impact loading from floating ice, ship and dropped objects. The authors develop a novel stainless steel-lightweight high ductility cement composite (LHDCC) beams in this study, which combine the advantages of LHDCC and stainless steel plates to provide superior impact performance. Ten full-scale stainless steel-LHDCC composite beams are designed with different stud spacing, concrete thickness, concrete types, stud types and number of core layers. Firstly, the compression performance of the LHDCC under complex stresses is verified by triaxial compression tests and the fitted equation for the triaxial compressive strength of LHDCC under triaxial stress state is also derived. Then, the study conducts impact tests to investigate the effect of different parameters on their performance deterioration under two impacts. The failure modes, impact force history, displacement history, velocity history, strain history and reaction force-displacement curve of the composite beam under two impacts are analyzed in detail. Based on the test results, the impact performance deterioration of the composite beam under two impacts is mainly reflected in the decrease of the global stiffness and average impact force as well as the increase of the maximum mid-span displacement. Finally, finite element (FE) simulation using LS-DYNA is carried out to investigate the impact response of the composite beams, in which the multi-drop hammer modeling method is proposed to simulate the two impacts scenario. Based on the results of the triaxial compression tests, the study provides a well-calibrated Continuous Surface Cap Model (CSCM) constitutive model for LHDCC to ensure the correctness of the simulation. The numerical results are in good agreement with the experimental results, which provides an efficient alternative solution to study the performance deterioration of the composite beam under two or multiple impacts. Based on the calibrated FE model, the energy absorbed by each component of the composite beams with different parameters under two impacts is quantified and analyzed in detail.

Corresponding author. Tel: +86-8697-5402; Fax: +86-2673-2850; Email: huangzhenyu@szu.edu.cn

Keywords: *Impact test, Fiber reinforced Concrete, Stainless steel, Continuous Surface Cap Model, Triaxial tests*

1. Introduction

For marine structures, the occurrence of collisions is not an isolated event and often presents a repeated impact scenario. Repeated impact with low velocity and large mass is of growing concern to structural engineers because this loading scenario is associated with most of the common accidental loading cases in marine structures. For ship and offshore structures, typical repeated impact scenarios include multiple impacts from ice floes, helicopter landings, and docking of supply ships[1-3], etc. Steel-concrete-steel (SCS) composite structures are composed of external steel plates and internal concrete and it is being widely used in offshore structures[4], immersed tube tunnels[5], protective structures[6] due to their high impact resistance and structural integrity. Researchers have conducted numerous experimental, numerical, and theoretical studies on the mechanical behavior of SCS composite structures under impact loading[7-12]. Liew and Sohel[7-8] et al. conducted drop hammer impact tests on SCS composite beams and slabs with J-hook connectors and quantified the effects of the parameters such as concrete thickness, connector diameter, concrete type, and fiber content on the impact response. The results showed that J-hook connectors effectively reduced the separation of the external steel plate from the concrete and improved load carrying capacity of the beams and slabs. Remennikov[9-10] et al. conducted impact tests on axially restrained SCS composite slabs and found that the membrane action of the steel plate can improve the resistance of the SCS slab. The finite element modeling simulated a vehicle impact scenario and the simulation results showed that the axially restrained SCS plate has highly impact resistance and effectively terminate the fast moving vehicle. Zhao[11-12] et al. performed drop hammer impact tests on SCS walls under axial compression. The effects of impact energy, axial pressure, steel plate thickness were investigated. It was shown that the residual bearing capacity of the SC wall under impact could be significantly reduced and the impact resistance of SC walls was very sensitive to the axial compression ratio when it exceeded 0.3.

In recent years, the development of computational techniques, numerical methods and material constitutive models has enabled more accurate simulation of structures under impact loads. The use of finite element (FE) software to predict structural responses of structures under dynamic loading is the most effective option due to the expensive impact experiments and the complexity of theoretical formulation. In a FE simulation, material constitutive parameters are essential to the accurate and correctness of the prediction results. The widely used concrete constitutive models for dynamic simulation, such as the concrete plastic damage model (K&C model) and the continuous surface cap model (CSCM), were developed primarily for ordinary concrete, which may not be suitable for modelling advanced cement composites. Therefore, to ensure the accuracy of simulations, the input parameters for new concrete materials have to be calibrated by experiments.

Xu[13] et al. calibrated the input parameters of the CSCM model for ultra-high performance concrete (UHPC) through uniaxial and triaxial tests, and used the calibrated parameters to build a FE model of UHPC filled thin-walled steel tubular. The FE results agreed well with the test results. Jia[14] et al. calibrated the input parameters of the CSCM for UHPC materials via material tests, including static tensile and compression tests, dynamic tensile and compression tests, and hydrostatic pressure tests on UHPC, and validated the model by experimental results. Wu[15] et al. studied the impact behavior of UHPC filled steel tube numerically, and further proposed the parameters for UHPC using the K&C model. Better predictions of the impact force and displacement responses have been obtained based on the proposed input parameters rather than using the default parameters. The structural response under repeated impact is different from that of a single impact. Repeated impact will cause multiple expansions of the plastic region of the structure and accumulation of deformation. Moreover, the residual stress and strain caused by the previous impact will affect the dynamic response of the structure during the subsequent impact. Therefore, the less sensitive parameters under a single impact may become more sensitive as the number of impacts increases. However, the current research on the impact performance of SCS structures is mainly focused on single impacts at high or low speeds, and less research has been reported on its impact performance deterioration mechanism under two impacts.

In the previous study, the author developed a stainless steel-lightweight concrete composite beam[16] with the following two main design features, i.e., (1) stainless steel was used as the external steel plate to prevent corrosion in the marine environment, (2) the developed lightweight high-ductility cement composite (LHDCC[17]) and rubberized LHDCC (RLHDC[18]) were used as the core material to improve the energy absorption behavior. The proposed composite structure is mainly used for impact- and explosion-resistant structures in harsh offshore environments, such as ship/vehicle impact/blast walls, security barriers for the offshore structures. Stainless steel has excellent ductility and strain-hardening properties, and can absorb considerable impact energy without fracture. In contrast to carbon steel which requires regular repainting and maintenance, stainless steel has high corrosion-resistant property, offering a low maintenance, lightweight solution for durability-related applications in marine environments. In addition, the stainless steels have been commonly used as structural components in seawater desalination plants, nuclear power plants, and petrochemical industries. [19]. Single impact tests have been conducted to investigate the dynamic responses of the proposed composite beam. In this paper, considering the continuity of impact load, the flexural performance deterioration of the stainless steel-lightweight concrete composite beam under two impacts is investigated. The effects of design parameters (connector spacing, connector type,

concrete thickness, concrete type, number of core layers and impacts) on the structural performance of the composite beam are analyzed. The input parameters of the CSCM constitutive model for LHDCC are calibrated by uniaxial tensile, compression tests and triaxial compression tests. A FE model for impact test is built by the multi-drop hammer modelling method in LSDYNA, which provides an effective alternative method for impact performance studies of composite beams.

2. Full-scale Experiment

2.1 Specimen design

Ten full-scale specimens are designed for the test, and the design details of the specimens are shown in Figure 1. Table 1 lists the geometric parameters of each specimen. The total length of each composite beam is 1200mm and the clear span is 875mm. The specimens are named by "concrete type-concrete thickness-stud spacing". For example, L-H125-S100 refers to LHDCC as core material with a concrete thickness of 125mm and stud spacing of 100mm. There are five design parameters, including stud spacing (100,150,200mm), concrete thickness (80,125,160mm), concrete types (LHDCC, RLHDC, NC (normal concrete), UHPC), types of stud (overlapped headed studs and short studs, as shown in Fig.1(b)) and number of core layers (single and double layer, as shown in Fig.1(b)). "U" in specimen "L-H125-S100(U)" represents the use of short studs, and "D" in "L-H160-S100(D)" represents double layer concrete. From Table 1, most of the specimens were designed as partial shear connection for economic and technical reasons. On the one hand, the partial shear connection can save cost compared to the complete shear connection. On the other hand, the specimen with partial shear connection exhibits more ductile behavior due to the bond-slip effect, which achieves larger enclose area of the load–displacement curve, showing relatively higher energy absorption capacity[20].

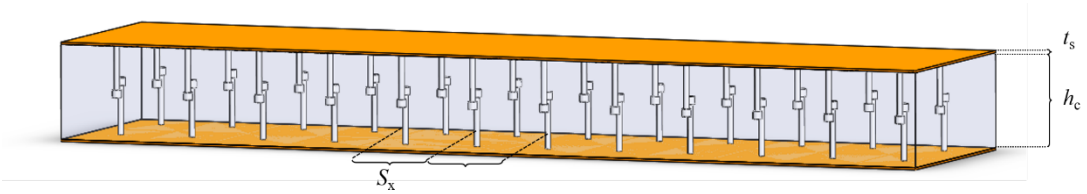

(a) Geometric parameters of specimen

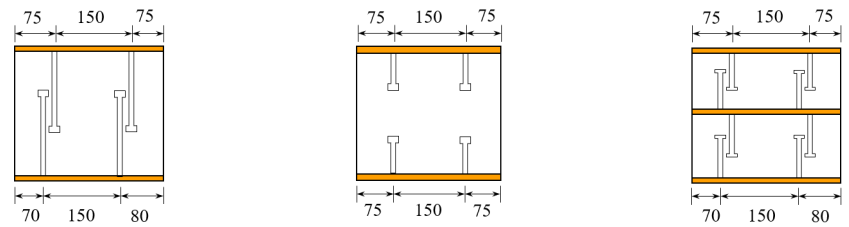

(b) Different cross-section of specimen

Fig.1 Design details of the specimen

Table 1 Parameters of the test specimens

Specimen	h_c(mm)	S_x(mm)	t_s(mm)	Core material	Connector	λ	ρ(%)	η
L-H125-S100	125	100	3	LHDCC	Overlapped	3.5	4.58	0.54
L-H125-S150	125	150	3	LHDCC	Overlapped	3.5	4.58	0.41
L-H125-S200	125	200	3	LHDCC	Overlapped	3.5	4.58	0.34
L-H80-S100	80	100	3	LHDCC	Overlapped	5.5	6.98	0.54
L-H160-S100	160	100	3	LHDCC	Overlapped	2.7	3.75	0.54
L-H125-S100(U)	125	100	3	LHDCC	Short	3.5	4.58	0.54
R-H125-S100	125	100	3	RLHDC	Overlapped	3.5	4.58	0.46
U-H125-S100	125	100	3	UHPC	Overlapped	3.5	4.58	1.00
N-H125-S100	125	100	3	NC	Overlapped	3.5	4.58	0.91
L-H160-S100(D)	80*2	100	2	LHDCC	Overlapped	2.7	3.75	0.54

Notes:h_c, S_x, t_s are the thickness of core concrete, studs spacing, and thickness of stainless steel plate, respectively; λ is the shear span to depth ratio and $\lambda = 2h_c/875$; ρ indicates the steel contribution ratio, $\rho = at_s/(at_s + h_c)$, a is the number of steel layers; η is the degree of shear connection $\eta = nP_s/f_y t_s B$; n, P_s, B are the stud number in the shear span, stud shear resistance and beam width; $P_s = \min(0.29\alpha_c d^2\sqrt{f_c E_c}, 0.8 f_u \pi d^2/4)$[21], $\alpha_c = 0.2(\frac{h_s}{d} + 1)$ for $3 \le \frac{h_s}{d} \le 4$, $\alpha = 1$ for $\frac{h_s}{d} > 4$; h_s, d are the overall nominal height and diameter of stud; f_c, E_c, f_u are cylinder compressive strength of concrete, elastic modulus of concrete, and tensile strength of studs.

Figure 2 shows the manufacturing process of the specimens. First, studs are welded on stainless steel plates, and the welded steel plates are assembled to obtain the steel skeleton of the composite beam. The concrete is then poured into the beam by a pump. The specimens are tested after curing for 28 days.

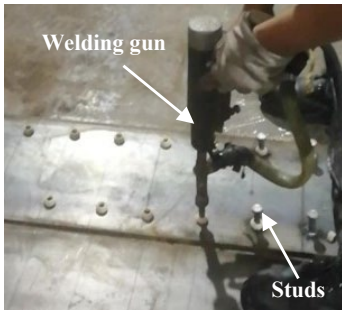

(a) Welding of studs

(b) Assemble as a frame

(c) Pumping concrete

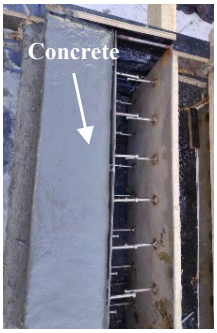

(d) Curing concrete

Fig.2 Specimen preparation process.

2.2 Materials

2.2.1 Concrete

The main concrete material used in this test is LHDCC, while UHPC, RLHDC and NC are also used in order to study the effect of different materials. The mix proportion of each material are shown in the previous study[16]. For uniaxial mechanical properties, tensile and compression tests are performed on concrete cylinders and coupons. Table 2 shows the test results for each material.

Table 2 Uniaxial mechanical properties of concrete

Concrete type	ρ_c(kg/m^3)	υ	E_c(GPa)	f_c'(MPa)	f_t(MPa)

LHDCC	1388	0.28	14.8	38.8	3.78
RLHDC	1203	0.33	13.2	30.1	3.34
UHPC	2765	0.25	46.1	126	6.61
NC	2438	0.24	34.2	44.8	-

Note: ρ_c, υ, E_c are the density, poisson ratio, and elastic modulus of the concrete; f_c' is the compressive strength of concrete cylinder; f_t is the tensile strength of concrete coupon.

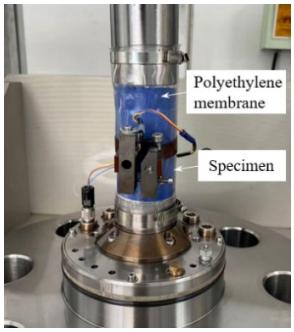

(a) Test set-up

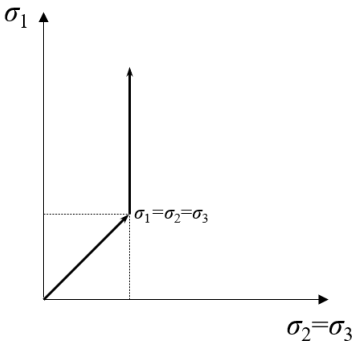

(a) Loading path

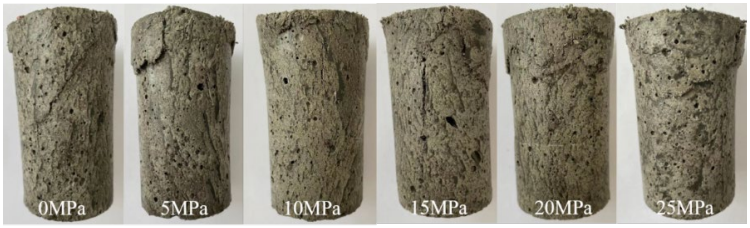

(c) Failure modes of triaxial compression tests

Fig.3 TXC test results

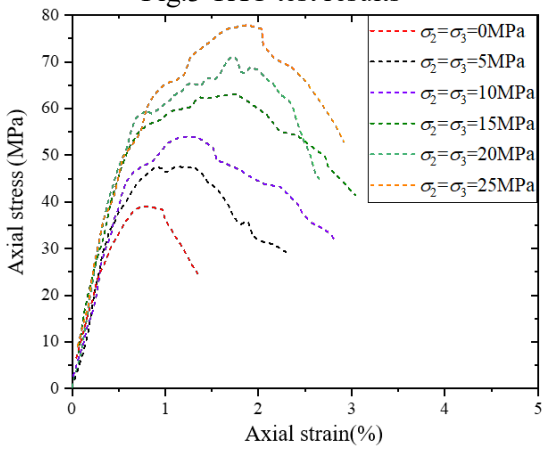

Fig.4 Axial stress-strain curves of triaxial compression tests

Table 3 Triaxial compressive strength of LHDCC.

Confined pressure (σ_2=σ_3)(MPa)	Peak axial stress σ_1(MPa)	Peak axial strain ε_1(%)
0	39.16	0.76
5	47.27	0.96
10	53.96	1.16
15	62.26	1.45
20	70.46	1.67
25	77.89	1.87

LHDCC is a lightweight porous material and its mechanical properties in triaxial condition are quite different from those of normal concrete. For the subsequent calibration of the constitutive parameters in section 4.2, its performance under complex stress condition is investigated by triaxial compression tests (TXC). Cylindrical specimens of Φ50×100 mm are prepared for the TXC tests, as shown in Fig.3(a). The tests are performed using a mixture of load-controlled and displacement-

controlled loading modes. First, the axial stress (σ_1) and radial stress (σ_2=σ_3) increases simultaneously at a rate of 0.1MPa/s to a desired confining pressure (0, 5, 10, 15, 20, 25MPa). Then, the axial stress (σ_1) increases at a rate of 0.01mm/s (keeping σ_2=σ_3 constant) until the specimen fails. The loading path of the TXC tests is shown in Fig.3(b). The failure patterns of the LHDCC under different confining pressures are shown in Fig.3(c). It can be found that the specimens without confining pressures have oblique cracks while those with confining pressures show vertical cracks. The stress-strain relationship of the TXC test is shown in Fig.4. The peak stress and strain of the LHDCC increases with the increase of the confining pressure, as shown in Table 3. It can be found that the relationship between the peak stress and the confining pressure is approximately linear. Eq.(1) is derived by the least squares method for the triaxial compressive strength of the LHDCC.

$$\frac{\tau_s}{f_c'} = 0.49 + 0.11\frac{\sigma_s}{f_c'} \quad (1)$$

where, normal strength $\sigma_s = I_1 = \sigma_1 + \sigma_2 + \sigma_3$, shear strength $\tau_s = \sqrt{J_2} = \sqrt{\frac{1}{6}(\sigma_1 - \sigma_2)^2 + (\sigma_2 - \sigma_3)^2 + (\sigma_3 - \sigma_1)^2}$.

2.2.2 Stainless steel

The external steel plate and the internal shear connectors of the composite beam are made of stainless steel with QN1803. QN1803 is a product developed by Qingtuo Group in 2019, with a reference to 304. It is characterized by low nickel content and cost savings [22]. Tensile tests are carried out on stainless steel plates and connectors, respectively. Fig.5 shows the tensile stress-strain curves of the steel plate and the shear stud. Since there is no obvious yield plateau in the tensile stress-strain curve of the stainless steel, the yield strength is taken as the stress corresponding to 0.2% of the residual strain. Table 4 shows the yield strength f_y and ultimate strength f_u of the stainless steel plate and stud.

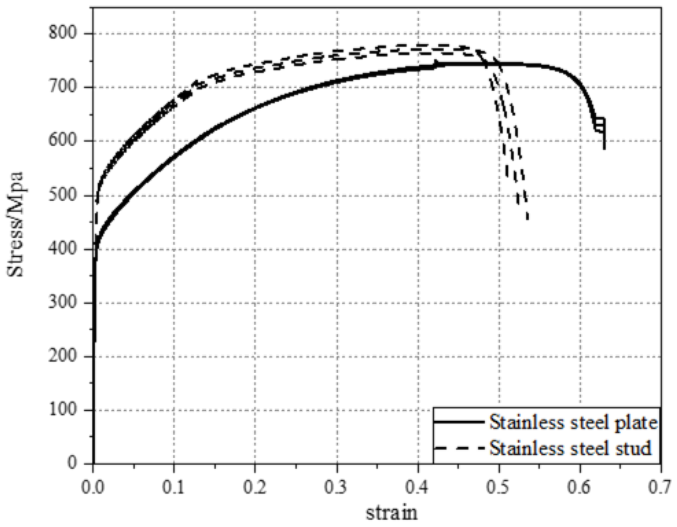

Fig.5 Tensile stress-strain curves of stainless steel

Table 4 Mechanical properties of stainless steel material

Specimen	E(GPa)	f_y(MPa)	f_u(MPa)
Steel plate	201.3	401.8	742.6
Stud	198.7	489.7	774.2

2.3 Test Set-up and Instrumentation

All specimens are impacted twice, and for each impact, a hammer with a mass of 512 kg is dropped from a height of 0.77 m to impact the specimen. The test setup for the impact tests is shown in Fig.6. The impact forces during the impact are recorded by the load cell at the hammer head, while the reaction forces are recorded by the load cell at the bottom of the beam. A high-speed camera is used to record the whole process of impact. The LVDT and strain gauges, as arranged in Fig.7, measure the displacement of the beam and the strain of the steel plate.

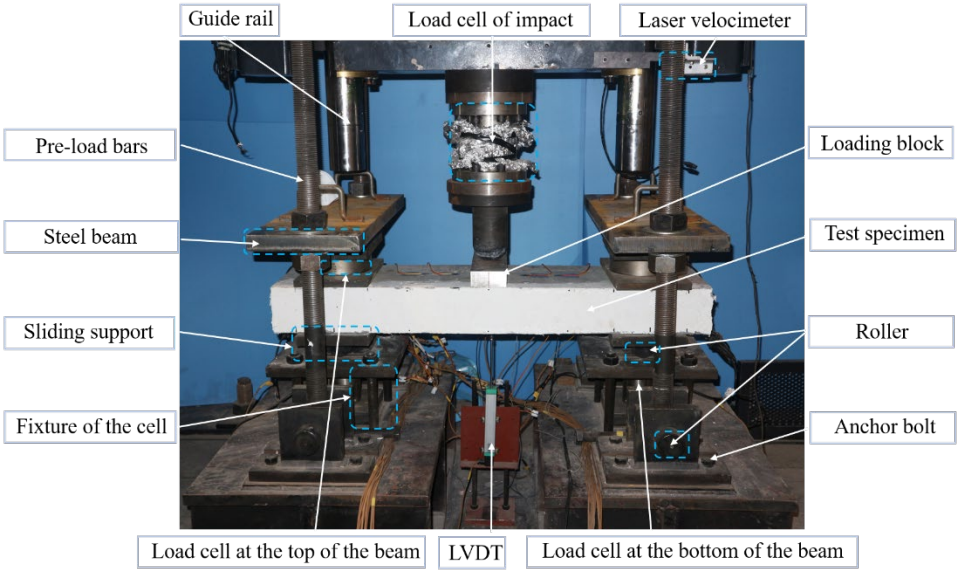

Fig.6 Test set-up for impact test

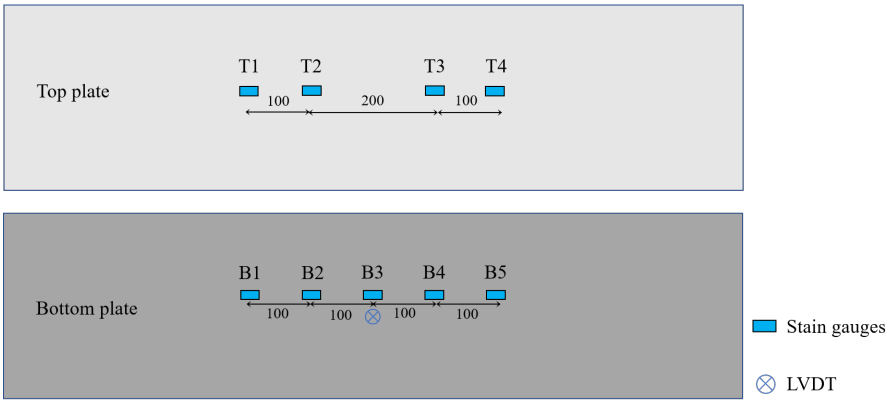

Fig.7 Arrangement of LVDT and strain gauges

3. Test Results and Discussions

3.1 Failure Modes

Three different failure modes occur in the composite beam under impact, i.e., flexural failure with bond-slip (L-H125-S100, L-H125-S150, L-H125-S200, L-H80-S100, L-H160-S100, L-H160-S100(D), L-H125-S100(U), R-H125-S100), flexural failure (U-H125-S100), and shear failure (N-H125-S100). Fig.8 illustrates the flexural failure with bond-slip. After the first impact, flexural cracks appear and concentrate in the middle of impact region. The interface between the steel plate and the concrete shows slippage, which is reflected at the end of the specimen. After the second impact, the width of the critical crack and the bond-slip are larger than those after the first impact, but no new flexural crack is generated. Especially in L-H125-S200, L-H80-S200 and L-H125-S100(U), a large number of studs attached to the bottom steel plate fracture and the bottom steel plate is separated from the concrete. The bond-slip and its magnitude after impact are shown in Fig.8(b). As the stud spacing increases from 100mm to 150mm and 200mm, the bond-slip under the first impact increases from 5.3mm to 7.9mm and 13.5mm and increases from 9.4mm to 15.1mm and 22.3mm under the second impact. Under the same steel ratio, the bond-slips of the double-layer specimen under the two impacts are, respectively, 2.8mm and 5.7mm, which are much smaller than those of the single-layer specimen.

Fig.9 shows the shear failure of specimen N-H125-S100. After the first impact, in addition to the mid-span flexural cracks, there are obvious shear cracks along the shear span. After the second impact, the shear cracks propagate further. The left side of the beam is broken into two parts, and the top steel plate buckles near the impact area.

Fig.10 shows typical flexural failure occurred in specimen U-H125-S100. After the first impact, a critical flexural crack appeared in the mid-span of the specimen while there is no bond-slip at the beam end. After the second impact, the main crack in the span extends upward significantly. After the two impacts, the integrity of the composite beam remains intact and there are no new cracks formed.

The reason for the different failure modes is that the concrete materials used as the core affect the degree of shear connection and shear resistance of the beams. The studs embedded in different concrete core have different shear resistance P_s, which will lead to different degrees of shear connection η. The specimens with a LHDCC cores have a low degree of shear connection (η<1.0) and are prone to slip at the steel-concrete interface, resulting in flexural failure with bond-slip. Compared to LHDCC and UHPC, the specimen with an NC core has lower shear resistance which is prone to shear failure. The specimen with a UHPC core has relatively higher compressive strength, which leads to a higher degree of shear connection (η=1.0) and structural integrity, resulting in flexural failure.

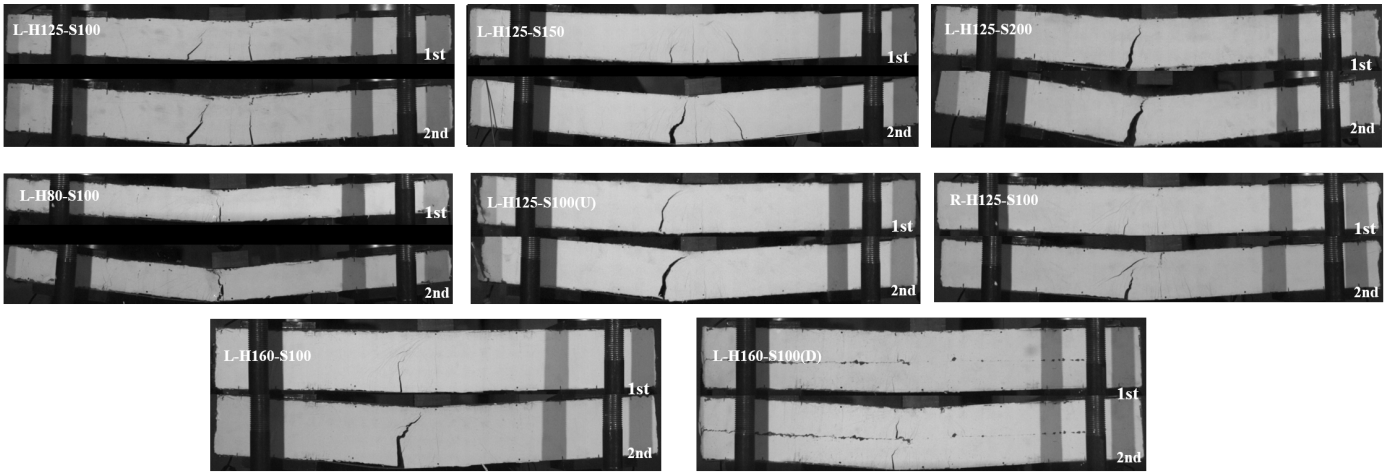

(a) Critical crack of specimen

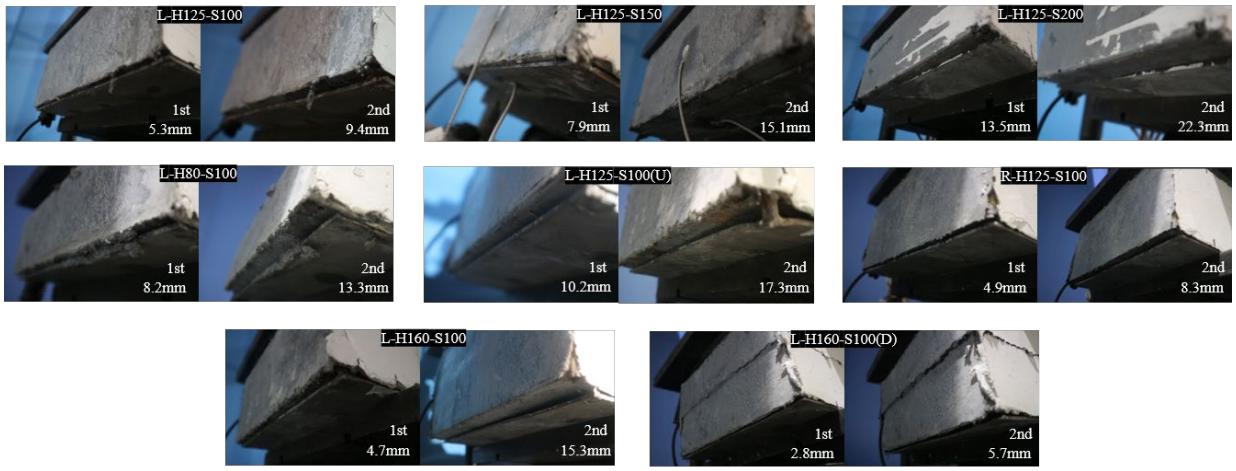

(b) Bond-slip of specimen

Fig.8 Flexural failure with bond-slip

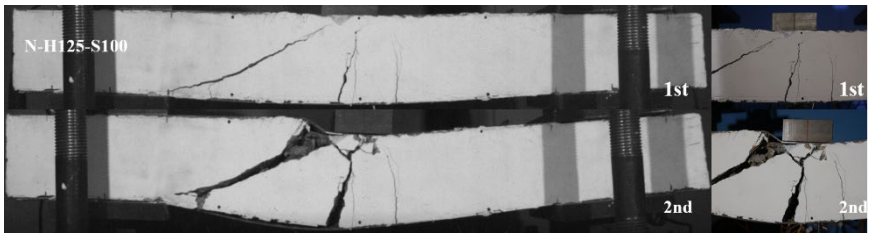

Fig.9 Shear failure

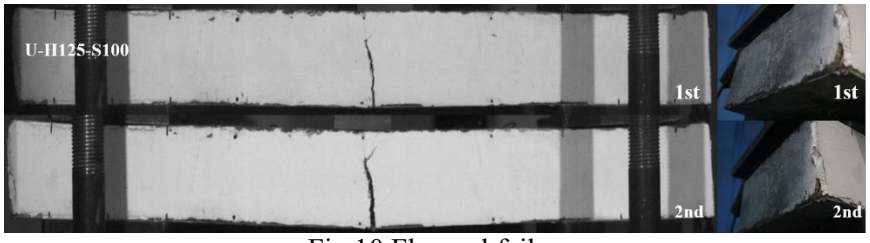

Fig.10 Flexural failure

3.2 Impact force history

The typical impact force-time curve of the composite beam under two impacts is shown in Fig.11 (Take L-H125-S100 for

example). The impact process is divided into three stages. (1) Inertial stage. At the beginning of the impact, the impact force reaches the peak P_{max} within 1ms. Since the stress wave has not transmitted to the support at this time, no reaction force is generated at this stage and the impact force is mainly balanced by the inertia force. (2) Loading stage. As the impact proceeds, the momentum of the hammer head is transferred to the beam which is deformed to a large extent. Due to the interaction between the hammer and the beam, the impact force appears to oscillate significantly[23]. The impact force is then gradually stabilized to form a plateau. It is worth noting that the impact force drops to zero at around 2~3ms. The reason is that the composite beam is accelerated to a velocity greater than the hammer after the inertial stage, resulting in the separation between the hammer and the specimen. (3) Rebound stage. The hammer bounces upward after the loading stage and the impact force gradually decreases to zero. The average impact force P_{ave} over the loading stage is defined by Eq.(2).

$$P_{\text{ave}} = \frac{\int_{t_1}^{t_2} P(t)dt}{t_2 - t_1} \tag{2}$$

where, P(t) is the impact force at time t; t_1, t_2 are the start time and end time of the loading stage, respectively.

Under the second impact, the shape of the impact force-time curve is similar to the first impact, but with relatively smaller peak impact force and impact plateau force. The reason is that the contact stiffness and bearing capacity of the beam are reduced after the first impact. P_{max} and P_{ave} under each impact are shown in Table 5. Fig.12 shows the effect of different parameters on P_{max} and P_{ave}. As the stud spacing increases from 100mm to 150mm and 200mm, P_{ave} under the first impact decreases by 10% and 51%, while P_{ave} under the second impact decreases by 12% and 56%, respectively. As the concrete thickness increases from 80 mm to 125 mm and 160 mm, P_{max} under the first impact increases by 23% and 40%, while P_{max} under the second impact increases by 19% and 21%, respectively. With the increase of concrete thickness from 80mm to 125mm and 160mm, P_{ave} increases by 60% and 91%, respectively, under the first impact, while increases by 88% and 135%, respectively, under the second impact. The definition of Δ_{pla} is the percentage reduction between P_{ave} (1st) and P_{ave} (2nd). It can be found that the specimen with double-layer core (L-H125-S100(D)) and the specimen with UHPC core (U-H125-S100) have the smallest Δ_{pla}. The reason is that the presence of a middle steel plate in the double-layer core specimen limits the development of the main crack in the concrete, thus maintaining a better integrity and structural resistance at the second impact. The UHPC specimen is a composite with complete shear connection (η=1.0) due to a much higher compressive strength (126MPa) of the concrete, thus, the bottom steel plate is fully utilized under both impacts, which is an important reason for a smaller Δ_{pla}.

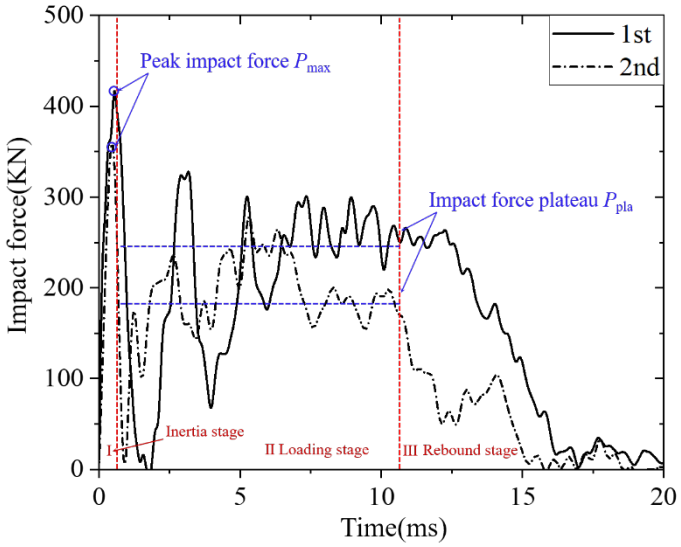

Fig.11 Impact force history of L-H125-S100

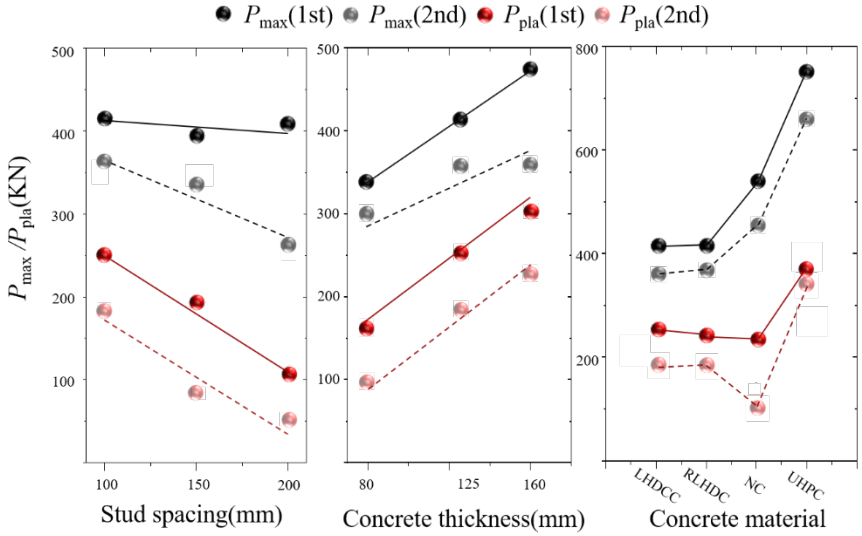

Fig.12 Effect of different parameters on impact force

3.3 Displacement/Velocity history

Fig.13 shows the mid-span displacement-time curve and the velocity-time curve of the composite beam under two impacts. The acceleration of the beam under impact is measured by the accelerometer arranged in the mid-span while the velocity time curves are obtained by integrating the data. When the hammer touches the beam, the velocity of the beam at the impact point rises abruptly, but there is no significant mid-span displacement at this moment. As the impact proceeds, the mid-span displacement increases and the velocity of the beam begins to decrease. The velocity-time curves keep oscillating afterwards due to the interaction between the hammer and the beam. When the velocity of the beam decreases to zero, the beam reaches the maximum mid-span displacement D_{max}. Then, the velocity becomes negative, i.e., it moves in the opposite direction, and the beam starts to rebound as well as recovering part of the deformation. Finally, the velocity of the beam fluctuates

around zero and the mid-span displacement stabilizes to a residual displacement D_{res}.

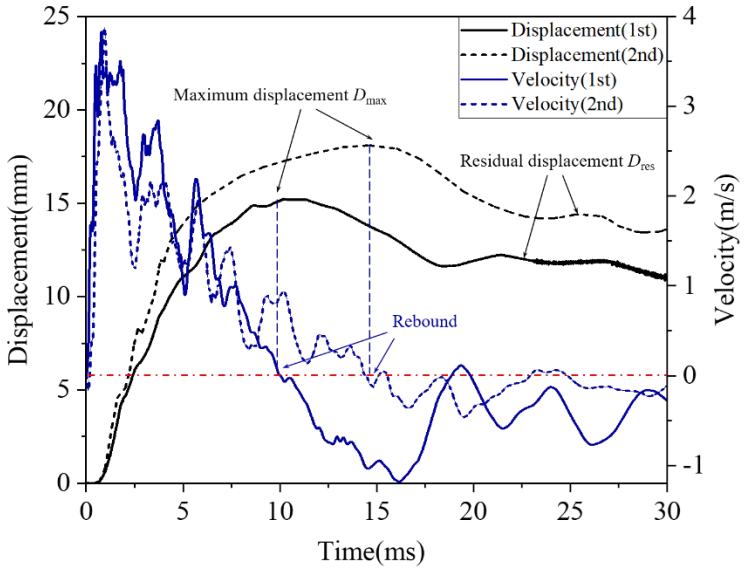

Fig.13 Mid-span displacement and velocity–time history of L-H125-S100

Fig.14 shows the effect of different parameters on D_{max} and D_{res}. Under the first impact, D_{max} increases by 23% and 67% while D_{res} increases by 25% and 91% with the increase of stud spacing from 100 mm to 150 mm and 200 mm, respectively. Under the second impact, D_{max} increases by 32% and 61% while D_{res} increases by 53% and 102%. With the increase of concrete thickness from 80mm to 125mm and 160mm, D_{max} decreases by 46 % and 54 %, respectively, under the first impact, and decreases by 46% and 48%, respectively, under the second impact. The displacement curve of the second impact has a larger mid-span displacement compared with that of the first impact. The reason is that the composite beam has been damaged after the first impact with the flexural stiffness being reduced, the displacement increases after the second impact with the same impact energy. However, the exceptions are specimen L-H160-S100(D) and U-H125-S100, whose second impact displacements D_{max} are slightly smaller than those after the first impact. This indicates that the impact resistance of these two specimens has not deteriorated significantly by the additional impact. This is attributable, as mentioned before, to that L-H160-S100(D) has a middle steel plate and U-H125-S100 has the complete shear connection. The definition of Δ_{max} is the percentage increase between D_{max} (1st) and D_{max} (2nd). Specimen N-H125-S100 has the largest Δ_{max}, which is because, compared to LHDCC and UHPC, normal concrete has lower tensile strength and ductility, and the concrete tends to spall under impact, leading to severe deterioration in the impact-resistance performance of the specimen.

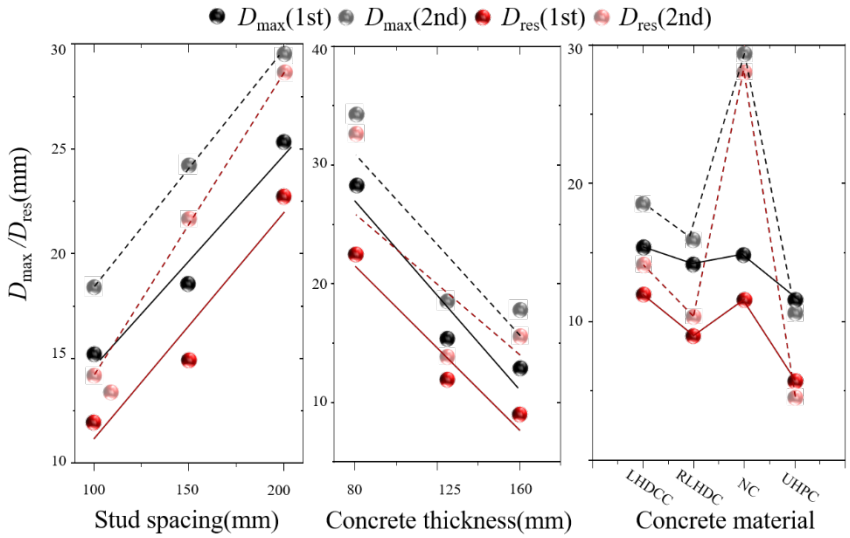

Fig.14 Effect of main parameters on displacement

3.4 Reaction force-displacement curves

Fig.15 shows the reaction force-displacement curves of the composite beam under two impacts. The reaction force increases with the increase of displacement, specified by dynamic global stiffness k. There is followed by some oscillations before reaching the maximum displacement. The hammer then bounces upward and the reaction force starts to unload. It can be found that the slope of the unloading curve is approximately equal to the loading slope k. The kinetic energy E_k of the hammer is completely converted into the internal energy of the beam when the composite beam reaches D_{max}. The energy absorbed in the form of the global deformation of the beam can be defined as E_w , as shown in Eq.(3). The energy absorbed by unit mass of the beam is defined as the specific energy absorption $E_s = E_w/M_b$

$$E_w = \int_0^{D_{max}} R(w)dw \tag{3}$$

where, R(w) is the reaction force at displacement w and D_{max} is the maximum displacement.

The k, E_w, E_s of the composite beam under two impacts are shown in Table 5. With the increase of stud spacing and the decrease of concrete thickness, the dynamic global stiffness k of the beam under two impacts gradually decreases. The deterioration of global stiffness Δ_k is more sensitive to concrete thickness. The ratio of energy absorbed by the beam to the impact energy E_w/E_k varies between 48% and 94%, indicating that most of the kinetic energy has been absorbed by the deformation of the beam. The relatively small E_w/E_k values of specimen L-H125-S200, L-H80-S100, and N-H125-S100 are due to their severe local failure, where part of the energy is dissipated by concrete crushing. Specimen R-H125-S100 has the maximum specific energy absorption due to the addition of 10% volume fraction of rubber powder, which enhances the

energy absorption capacity during impact. Although specimen U-H125-S100 has superior impact-resistance performance (minimum D_{max} and maximum k), its specific energy absorption E_s is the smallest due to its large self-weight.

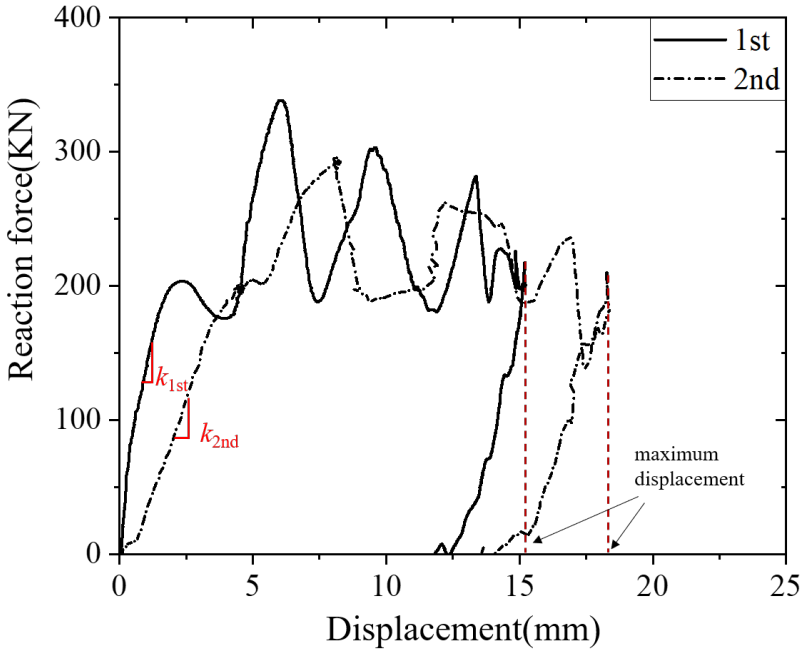

Fig.15 Reaction force-displacement curves of L-H125-S100

3.5 Strain history

Fig.16 shows the mid-span strain curves of the bottom steel plate and the failure modes after two impacts. For comparisons, the curves are plotted in the same figure, and the starting strain of the second impact is the residual strain of the first impact. At the first impact, the maximum strain of the bottom plate of L-H125-S100/150/200, which shows flexural failure with bond-slip, does not reach the yield strain of the steel (4840με) because the partial shear connection (η<1.0) resulted in an inadequate number of studs in the bottom plate. At the second impact, those specimens have smaller strains compared to those from the first impact due to the damage caused by the first impact (some studs have yielded or been broken). For the shear failure specimen N-H125-S100, the strain of the bottom plate is also relatively small. This is because the concrete cracks due to the low tensile strength during impact, and the studs embedded in the concrete cannot transfer the shear force, thus limiting the strain development of the bottom steel plate. For the flexural failure specimen U-H125-S100, the bottom steel plate has yielded at the first impact, and the strain continues to increase at the second impact. The specimen has a shear connection degree of 1.0 (η=1.0), which has full composite interaction. After the two impacts, the integrity remains intact, which allows the steel plate to be fully utilized, thus, generating strain-hardening under the second impact.

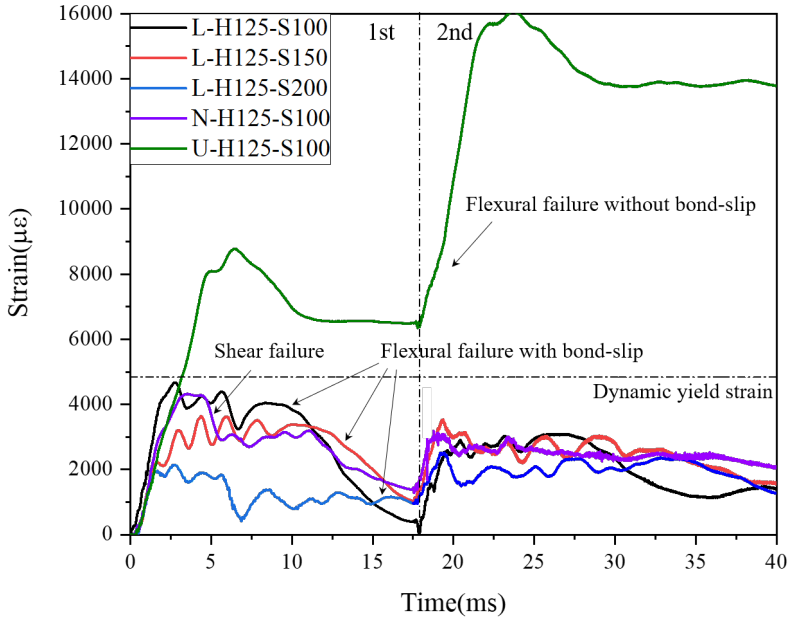

Fig.16 Strain curves for different failure modes during impact

Table 5 Test results under two impacts

Specimen	Impact Parameters				P_{max}	P_{ave}	Δ_{pla}	D_{max}	D_{res}	Δ_{max}	k	Δ_k	E_w	$\frac{E_w}{E_k}$	E_s	Failure mode
	i	M	v	E_k												
L-H125-S100	1	512	3.85	3795	415.1	236.2	22%	15.2	11.9	21%	85.5	18%	3497	92%	44.2	I
	2	512	3.84	3775	356.4	184.6		18.4	14.2		70.3		3137	83%	39.7	I
L-H125-S150	1	512	3.86	3814	393.4	212.3	23%	18.7	14.9	29%	80.1	12%	3253	85%	41.1	I
	2	512	3.86	3814	343.5	163.1		24.2	21.7		70.4		3084	81%	39.0	I
L-H125-S200	1	512	3.86	3814	407.8	115.8	29%	25.4	22.7	17%	69.9	28%	2567	67%	32.5	I
	2	512	3.84	3775	265.2	82.3		29.6	28.7		50.1		2250	60%	28.4	I+IV
L-H80-S100	1	512	3.83	3755	337.8	147.7	33%	28.3	22.4	21%	40.7	49%	2358	63%	41.7	I
	2	512	3.84	3775	298.5	98.3		34.2	33.0		20.7		2074	55%	36.6	I+IV
L-H160-S100	1	512	3.83	3755	474.5	282.6	18%	12.9	8.9	38%	111.05	19%	3340	89%	34.5	I
	2	512	3.81	3716	359.6	230.5		17.8	15.7		90.4		2935	79%	30.3	I
L-H125-S100(U)	1	512	3.82	3736	370.8	231.6	28%	18.2	14.4	15%	78.5	31%	2786	75%	35.2	I
	2	512	3.82	3736	304.5	167.8		20.9	18.1		54.3		2714	73%	34.3	I+IV
R-H125-S100	1	512	3.84	3775	416.4	255.7	26%	14.2	9.0	12%	80.4	22%	3515	93%	49.6	I
	2	512	3.82	3736	368.2	189.8		15.9	10.4		62.6		3144	84%	44.4	I
U-H125-S100	1	512	3.81	3716	751.6	369.6	8%	11.2	5.4	-4%	161.6	3%	3483	94%	24.7	II
	2	512	3.81	3716	658.3	341.3		10.8	5.0		156.3		3427	92%	24.3	II
N-H125-S100	1	512	3.83	3755	540.2	141.8	19%	14.8	11.6	86%	76.8	39%	2310	62%	18.3	III
	2	512	3.84	3775	456.8	115.2		27.6	29.5		46.7		1795	48%	14.2	III+V
L-H160-S100(D)	1	512	3.86	3814	495.1	308.6	10%	14.2	7.6	-2%	110.5	3%	3575	94%	36.9	I
	2	512	3.86	3814	414.2	277.3		13.9	7.1		106.7		3548	93%	36.7	I

Note: i = impact number; M = impact mass (kg); v = impact velocity (m/s) (Measured by velocimeter); Impact energy $E_k = 0.5MV^2$ (J); P_{max} = peak impact force (kN); P_{ave} = average impact force (kN); $\Delta_{pla} = (P_{ave,1st}-P_{ave,1st})/P_{ave,1st}\times100\%$; D_{max} = maximum mid-span displacement (mm); D_{res} = residual mid-span displacement (mm); $\Delta_{max} = (D_{res,2nd}-D_{res,1st})/D_{res,1st}\times100\%$; k = dynamic global stiffness (kN/mm); $\Delta_k = (k_{1st}-k_{2nd})/k_{1st}\times100\%$; E_w = energy absorbed by deformation (J); Specific energy absorption $E_s = E_w/M_b$ (J/kg), M_b = mass of beam; I = flexural failure with bond-slip; II = flexural failure; III = shear failure; IV = shear stud rupture (attached to bottom plate); V = top steel plate buckling.

4. Numerical Investigation

4.1 FE modeling

The frequently used method in performing numerical simulations for two or multiple impacts is the restart method[24]. The restart method requires modifying the k-file to use the calculation results of the previous impact as the initial conditions for the next impact. In order to simplify the simulation steps for two impacts, this study defines two drop hammers in a single k-file to impact the composite beam from different heights simultaneously to achieve the two impacts simulation, as shown in Fig.17. The distance between the two drop hammers is designed for the purpose of two impacts, which enables the second drop hammer impact the specimen after the first drop hammer impact ends. The acceleration of gravity and the height and initial velocity of each drop hammer need to be set in the numerical model. No contact is set between the two drop hammers, so that they do not affect each other.

In order to improve the computational efficiency, a quarter FE model is built and symmetric boundaries are applied. Solid elements (*ELEMENT_SOLID) are defined in the model for the drop hammer, concrete, studs and supports, and thick-shell elements (*ELEMENT_TSHELL) are used for the steel plates. The overlapped headed studs are simplified to straight bars of equal diameter and connected by spring elements (*ELEMENT_DISCRETE). The constitutive model of the spring elements is obtained by pull-out tests[16] and defined by the keyword *SPRING-NONLINEAR-ELASTIC, as shown in Fig.17. The mesh size affects the calculation accuracy and efficiency of the FE model. Based on the mesh sensitivity analysis, the mesh size of concrete and steel plate was determined to be 5mm. For the hammer and support with larger stiffness, a coarser mesh size of 10 mm was adopted, while for the shear connectors with complex stress, the mesh size was refined to 2 mm globally.

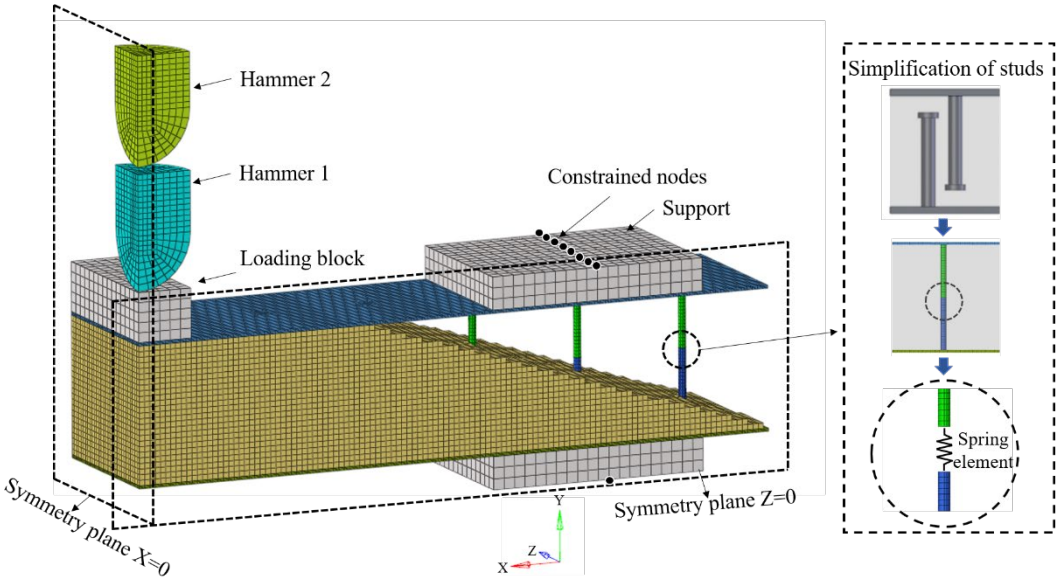

Fig.17 Quarter model of composite beam under two impacts

4.2 Calibration of material constitutive model

4.2.1 Modelling of LHDCC

The Continuous Surface Cap Model (CSCM) was developed by the Federal Highway Administration mainly to simulate the response of protective structures in vehicle crash[25].The model takes into account the shear dilation, strain-softening, and strain rate effects of concrete materials, which can simulate dynamic response of reinforced concrete under low-velocity impacts[26].The failure surface function of the model is defined as follows.

$$f(I_1,J_2,J_3) = I_2 - R^2F_f^2F_c \tag{3}$$

where I_1, J_2, J_3 are the first invariant of stress tensor, the second and third invariant of stress deviator tensor, respectively; R is the Rubin three-invariant reduction factor[25]; F_f, F_c are the failure surface function and hardening cap surface function. The compression meridian equation of the failure surface is as follows.

$$F_f(I_1) = \alpha - \lambda\exp(-\beta I_1) + \theta I_1 \tag{4}$$

where, α, β, λ, and θ are the parameters of the compression meridian, which can be determined by triaxial compressive tests. More details related to the CSCM model can be found in the literature[25-26]. The CSCM parameters for normal concrete are automatically generated after inputting uniaxial compressive strength $f_c^{'}$ and aggregate size D_{agg} in LS-DYNA. However, there is no coarse aggregate in LHDCC and its mechanical properties, especially under multiaxial loading conditions, differ from those of normal concrete. Therefore, it is necessary to calibrate its constitutive input parameters by triaxial tests. according to the LS-DYNA user manual[25] and related literature[13-15]. The calibration process is as follows.

In CSCM, the strength of a material is mainly presented by its failure surface, and the general shape of the three-dimensional failure surface is determined by the compressive meridian, tensile meridian and shear meridian. The function of the compressive meridian of the failure surface is given by Eq.(4), and the coordinates of the control points are shown in Fig.18(a). The four control points correspond to different typical states of stresses: Point A represents the triaxial tension state ($-3f_{tt}$, 0); Point B represents the biaxial tension state ($-2f_{bt}$, $f_{bt}/\sqrt{3}$); Point C represents the uniaxial compression state (f_c', $f_c'/\sqrt{3}$); and Point D represents the triaxial compression state ($\sigma_1+2\sigma_3$, $(\sigma_1-\sigma_3)/\sqrt{3}$). The triaxial tensile strength f_{tt} (equal tension in three directions) and the biaxial tensile strength f_{bt} are approximately equal to the uniaxial tensile strength f_t[27].The uniaxial compressive strength f_c' is taken from the results of the material properties test in section 2.2. σ_1 and σ_3 are the axial and radial compressive stress in the triaxial compression (TXC) tests, and Eq.(1) is fitted from the triaxial compression test results. The ultimate stress of LHDCC in any triaxial compression state is obtained according to Eq.(1). Three triaxial compression fitting points (D_1, D_2, D_3) are obtained by taking I_1 as 0.5 f_c', 1.5 f_c', 3 f_c', respectively. A total of six fitting points (A, B, C, D_1, D_2, D_3) are fitted to Eq.(4) by the least squares method to obtain the compression meridian parameters α, β, λ, θ. The fitted results for the compression meridian of LHDCC are shown in Fig.19. It can be found that the compression meridian of LHDCC is significantly different from that of normal concrete. Obviously, the uncalibrated CSCM parameters overestimate the strength of LHDCC under triaxial stress.

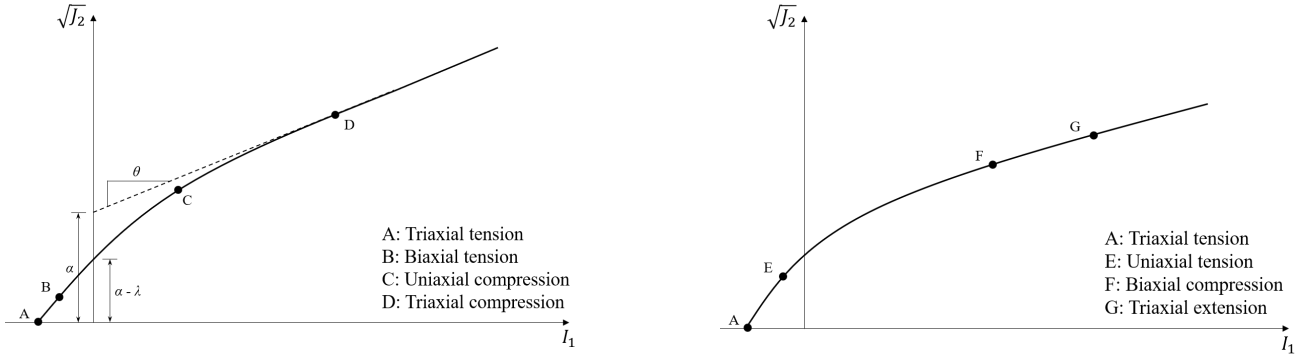

(a) Compressive meridian line (b) Tensile meridian line

Fig.18 Compressive and tensile meridian lines of the failure surface

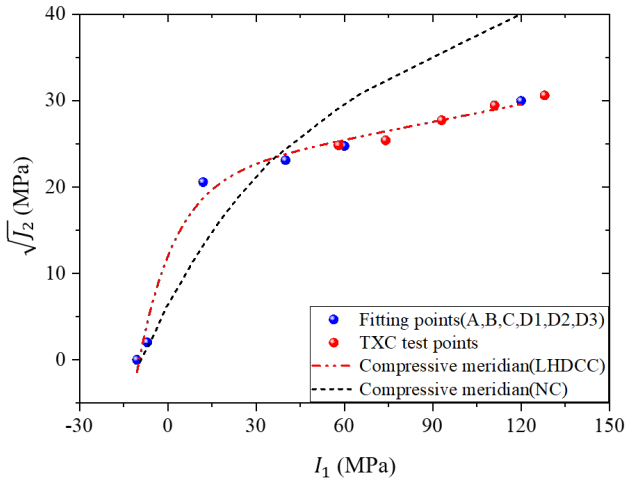

Fig.19 Compression meridian fitting results

341

342 The tensile meridian of the failure surface is shown in Fig.18(b). The coordinates of its control points are: Point A for the
343 triaxial tension state ($-3f_{tt}$, 0); Point E for the uniaxial tensile state ($-f_t$, $f_t/\sqrt{3}$); Point F for the biaxial compression state
344 (f_{bc}', $f_{bc}'/\sqrt{3}$); and Point G for the triaxial extension state ($\sigma_1+2\sigma_3$, $(\sigma_3-\sigma_1)/\sqrt{3}$). To the authors' best knowledge, the
345 function of the tensile meridian is not available in the literature. However, the tensile meridian function can be scaled by
346 the function of the compressive meridian using the Rubin scaling function(Q_2), i.e., $F_{ft}=Q_2F_f$, F_{ft}, F_f are the tensile and
347 compressive meridian functions, and the Rubin scaling function Q_2 is shown in by equation (5):

348 $$Q_2 = \alpha_2 - \lambda_2 \exp(-\beta_2 I_1) + \theta_2 I_1 \tag{5}$$

349 α_2, β_2, λ_2, θ_2 in the scaling function are the input parameters that need to be calibrated. In the above control points, f_t is the
350 uniaxial tensile strength available from the results of the material tests in section 2.2. f_{bc}' is the biaxial compressive strength
351 of concrete, which is taken as 1.16 f_c' for LHDCC[28].Compared to compressive strength, tensile strength of concrete is
352 relatively small, and there is no test data for triaxial extension tests of LHDCC in the literature. It is assumed, therefore, that
353 the triaxial extension properties of LHDCC are the same as those of normal concrete. The triaxial extension strength is taken
354 from the test results of Mills and Zimmerman[29]:

355 $$\frac{\tau_0}{f_c} = \frac{0.147+0.550\sigma_0}{f_c} \tag{6}$$

356 where,$\tau_0 = \sqrt{2J_2/3}$; $\sigma_0 = I_1/3$. The ultimate stress of concrete in triaxial extension state is obtained according to Eq.(6).
357 Taking I_1 as 0.5 f_c', 1.5 f_c', 3 f_c', respectively, three fitting points (G_1, G_2, G_3) of triaxial extension state are obtained. Ac-
358 cording to $F_{ft}=Q_2F_f$, a total of six control points (A, E, F, G_1, G_2, G_3) are fitted by the least square method based on Eq.(5)

to obtain the tensile meridian parameters α_2, β_2, λ_2, θ_2. In addition, Q_2=0.5 when I_1=0 is considered to ensure a smooth transition between the tensile and compression regions[25].

The shear meridian is located between the tensile meridian and the compressive meridian, which can be determined by the Rubin scaling function Q_1, as shown in equation (7):

$$Q_1 = \alpha_1 - \lambda_1 \exp(-\beta_1 I_1) + \theta_1 I_1 \tag{7}$$

The ratio of shear meridian to compression meridian Q_1 is 0.5774 when the hydrostatic pressure I_1 is 0[30], while other stress states (such as taking I_1 as 0.5 f_c', 1.5 f_c', 3 f_c') can be determined by Willians-Warnke function[25], shown in Eq.(8). The shear meridian parameters α_1, β_1, λ_1, θ_1 can be obtained by fitting Eq.(7).

$$Q_1 = \frac{\sqrt{3}(1-Q_2^2)+(2Q_2-1)\sqrt{3(1-Q_2^2)+5Q_2^2-4Q_2}}{3(1-Q_2^2)+(1-2Q_2)^2} \tag{8}$$

From the above calibration process, the modeling parameters for LHDCC are obtained and shown in Table 6.

Table 6 Failure surface modeling parameters for LHDCC

Parameter	α(MPa)	β(MPa^{-1})	λ(MPa)	θ	α_1	β_1(MPa^{-1})
value	21.547	8.327e^{-2}	9.526	7.601e^{-2}	0.747	5.852e^{-2}
Parameter	λ_1	θ_1(MPa^{-1})	α_2	β_2(MPa^{-1})	λ_2	θ_2(MPa^{-1})
value	0.170	8.531e^{-4}	0.660	5.486e^{-2}	0.160	1.019e^{-3}

4.2.2 Stainless steel

The stainless steel plate and studs in the composite beam are defined using *MAT-PLASTIC-KINEMATIC with the input parameters including modulus of elasticity E, yield stress f_y, tangent modulus E_t and failure strain F_s. The engineering stress-strain curve from the tensile test in Section 2.2 is converted to a true stress-strain curve by using Eq.(9). The failure strain F_s for stainless steel plates and studs is taken as 0.5 and 0.3, respectively[16].

$$\sigma_s = S(1+e); \varepsilon_s = \ln(1+e) \tag{9}$$

where, S and e are the engineering stress and strain, and σ_s and ε_s are the true stress and true strain. The strain rate of the steel is considered by the Cowper-Symonds model as follows.

$$f_y^d / f_y^s = 1 + (\dot{\varepsilon}/D)^{\frac{1}{p}} \tag{10}$$

where, f_y^d, f_y^s, $\dot{\varepsilon}$ are dynamic and static yield strengths and strain rates, respectively; D, p are strain rate parameters. For stainless steel materials, D, p are taken as 40.4s^{-1}, 0.5, respectively[31].

For other components such as drop hammer and steel supports, *MAT_ELASTIC is used to define the material properties due to its small deformation during impacts. The input parameters for the material of each component are shown in Table 7.

Table.7 Key parameters for steel

Part	Parameter
Hammer	E=200GPa, υ=0.27
Support	E=200GPa, υ=0.27
Steel plate	E=201GPa, υ=0.27, f_y =401MPa, E_t=1878MPa, F_s=0.5
Stud	E=198GPa, υ=0.27, f_y =489MPa, E_t =1878MPa, F_s=0.3

4.3 Contact definition and boundary conditions

This section defines the contact behavior between the parts by the keyword *CONTACT-AUTOMATIC-SURFACE TO SURFACE. The contact parameters FS and FD are static and dynamic friction coefficients, SFS and SFM are master and slave penalty stiffness coefficients, and different contact parameters are defined for different contact pairs. The values of the penalty stiffness between the hammer and the loading plate have a great influence on the peak impact force[32]. Therefore, trial and error are performed to determine the best possible values of the SFS and SFM between each contact pair, as shown in Table 8.

Table.8 Contact parameters

Contact	FS	FD	SFS	SFM
Hammer-Block	0.3	0.2	0.2	0.2
Plate-Concrete	0.7	0.5	0.15	0.15
Stud-Concrete	0.7	0.5	0.15	0.15
Plate-Support	0.3	0.2	0.2	0.2

To improve the calculation efficiency, symmetric boundary is applied on the XOY plane and the YOZ plane. As shown in Fig.18. All nodes in the XOY plane are selected by keyword *SET-NODE. The displacement in the Z-direction, the rotation in the X-direction and the Y-direction of selected nodes are constrained by keyword *BOUNDRY-SPC-SET. The nodes at the bottom of the support are restrained from any linear motion, while rotation along its centerline is allowed to simulate the simple support condition.

4.4 FE Results and discussions

Fig.21 shows the failure mode of the composite beam in FE results after two impacts. The comparison shows that the FE simulation can capture the location of the critical crack and reflect the failure pattern of the specimen. Table 9 shows the comparison of P_{max}, P_{ave}, D_{max} and D_{res} between FE and test results. The mean and standard deviation of the ratio of FE/Test for P_{max}, P_{ave}, D_{max} and D_{res} are 1.05 and 0.04, 1.05 and 0.03, 1.00 and 0.06, 0.96 and 0.12, respectively. The comparison of the impact force and displacement-time curves after two impacts is shown in Fig.20. It can be found that the FE results after the first impact is in good agreement with the test results, while the impact response of some specimens (such as L-H80-S100, N-H125-S100) after the second impact is slightly different from the FE results. The reason is that these specimens are severely damaged under the second impact. The damage pattern is asymmetric, i.e., the left span is severely damaged while the left part is relatively light. Therefore, there will be some deviation from the FE results for symmetric modeling.

Table 9 Comparison of FE results with test results

Specimen	Impact number	P_{max}(KN)			P_{ave}(KN)			D_{max}(mm)			D_{res}(mm)		
		TEST	FEM	T/F	TEST	FEM	T/F	TEST	FEM	T/F	TEST	FEM	T/F
L-H125-S100	1	415.1	441.4	1.06	236.2	243.3	1.03	15.2	16.9	1.11	11.9	11.8	0.99
	2	356.4	363.5	1.02	184.6	192.0	1.04	18.4	18.6	1.01	14.2	12.2	0.86
L-H125-S150	1	393.4	441.9	1.12	212.3	225.0	1.06	18.7	20.4	1.09	14.9	14.2	0.95
	2	343.5	364.1	1.06	163.1	176.1	1.08	24.2	23.7	0.98	21.7	19.7	0.91
L-H125-S200	1	407.8	437.8	1.07	115.8	129.7	1.12	25.4	24.9	0.98	22.7	22.2	0.98
	2	265.2	286.4	1.08	82.3	90.5	1.1	29.6	29.9	1.01	28.7	26.7	0.93
L-H80-S100	1	337.8	358.8	1.06	147.7	156.6	1.06	28.3	26.0	0.92	22.4	21.3	0.95
	2	298.5	307.5	1.03	98.3	106.2	1.08	34.2	31.1	0.91	33	29.0	0.88
L-H160-S100	1	474.5	521.3	1.10	282.6	291.1	1.03	12.9	14.2	1.10	8.9	11.2	1.26
	2	359.6	363.2	1.01	230.5	244.3	1.06	17.8	17.1	0.96	15.7	13.5	0.86
L-H125-S100(U)	1	370.8	406.6	1.10	231.6	224.7	0.97	18.2	18.4	1.01	14.4	11.2	0.78
	2	304.5	298.4	0.98	167.8	171.2	1.02	20.9	20.3	0.97	18.1	17.4	0.96
R-H125-S100	1	416.4	450.5	1.08	255.7	258.3	1.01	14.2	15.2	1.07	9	10.5	1.17
	2	368.2	375.6	1.02	189.8	201.2	1.06	15.9	16.2	1.02	10.4	9.6	0.92
U-H125-S100	1	751.6	736.3	0.98	369.6	377.0	1.02	11.2	11.3	1.01	5.4	6.4	1.19
	2	658.3	724.1	1.10	341.3	365.2	1.07	10.8	11.1	1.03	5	4.8	0.96
N-H125-S100	1	540.2	602.9	1.12	141.8	147.5	1.04	14.8	14.2	0.96	11.6	10.3	0.89
	2	456.8	470.5	1.03	115.2	121.0	1.05	27.6	25.7	0.93	29.5	28.3	0.96
L-H160-S100(D)	1	495.1	495.6	1.00	308.6	311.7	1.01	14.2	13.8	0.97	7.6	6.8	0.89
	2	414.2	430.8	1.04	277.3	285.6	1.03	13.9	14.3	1.03	7.1	6.5	0.91
Mean	-	-	-	1.05	-	-	1.05	-	-	1.00	-	-	0.96
Std.	-	-	-	0.04	-	-	0.03	-	-	0.06	-	-	0.12

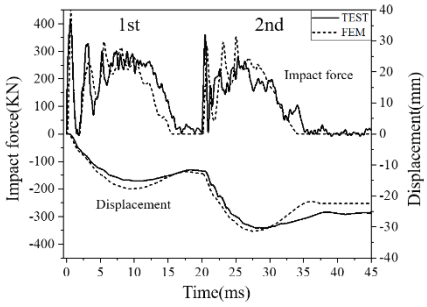

(a) L-H125-S100

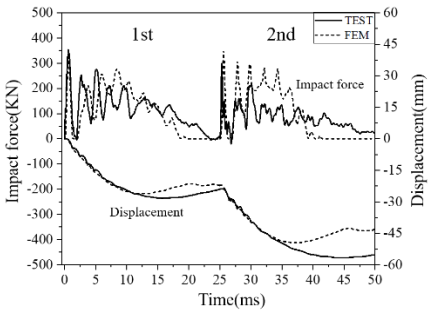

(b) L-H80-S100

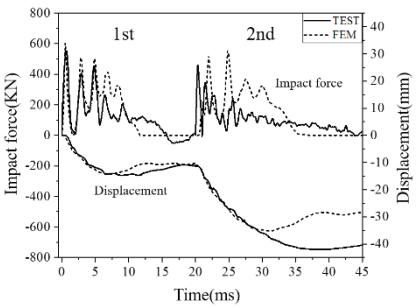

(a) N-H125-S100

Fig.20 Comparison of FE and test results(impact force/displacement history)

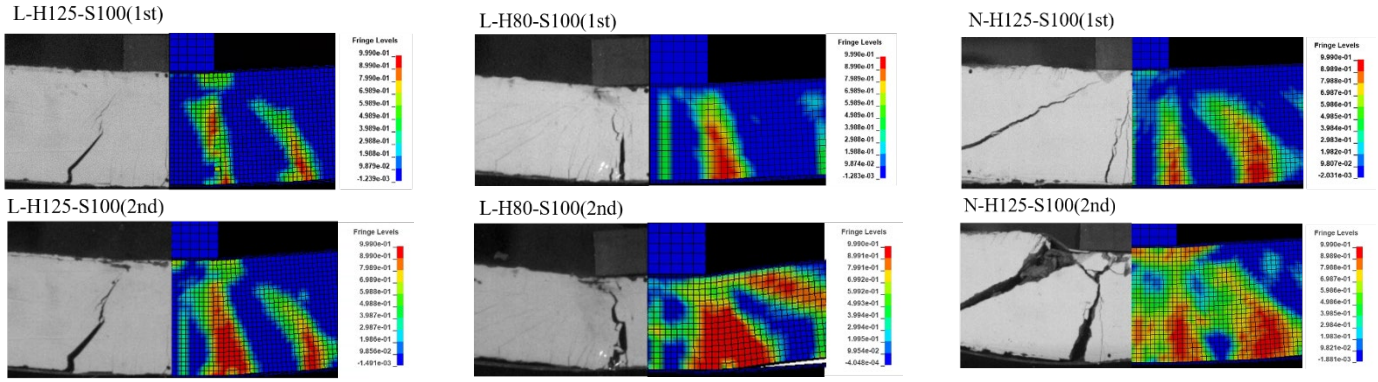

(a) L-H125-S100 (b) L-H80-S100 (a) N-H125-S100

Fig.21 Comparison of FE and test results(failure mode)

The kinetic energy of the hammer is absorbed by the composite beam and converted into internal strain energy stored in the steel plates, studs and concrete. The internal energy of each component can be output by the keyword *MATSUM from the FE model and summarized in Table 10. During the first impact, the energy is mainly absorbed by the concrete for the specimens showing flexural failure with bond-slip and shear failure, and by the steel plates for the specimens showing flexural failure. In the impact test, large strains occur in the steel plates of the flexural failure specimen, suggesting that the plates have absorbed more energy. However, the steel plate stresses in the specimens of the other two failure modes do not reach the dynamic yield strength, thus, impact energy dissipation are mainly attributed to plastic deformation and damage of the concrete. When the stud spacing increases from 100mm to 150mm and 200mm, the energy absorbed by the steel plates decreases from 43.5% to 37.1% and 31.4%, respectively. This is in consistent with the test results. The measured strain of the bottom steel plate decreases with the increase of the stud spacing, indicating that with a larger stud spacing, the bottom steel plate contributes less in resisting deformation and absorbing energy. As the concrete thickness increases from 80mm to 125mm and 160mm, the energy absorbed by the concrete increases from 36.2% to 40.6% and 53.8%, respectively. Compared to the specimen with short studs, the energy absorbed by the overlapped studs increases. Under the second impact, the energy absorbed by the concrete is greater than that absorbed during the first impact. For all the specimens except L-H160-S100(D) and U-H125-S100, the energy absorbed by the concrete accounts for more than 60%. It is noteworthy that, under the first impact, the energy absorbed by the steel plate in the single-layer specimen accounts for 30.8%, while it decreases to 9.6% under the second impact. However, with the same steel ratio, the energy absorbed by the steel plate in the double-layer specimen under both impacts exceeds 35%. It indicates that the impact resistance of the single-layer

specimen deteriorates under two impacts, resulting in a partially functioning steel plate under subsequent impacts. All the evidences have shown that the double-layer specimen has superior impact resistance.

Table 10 Energy absorption for each component in FE results

Specimen	Impact number	Concrete		Steel plates		Studs	
		Energy(J)	Proportion(%)	Energy(J)	Proportion(%)	Energy(J)	Proportion(%)
L-H125-S100	1	1346	40.6%	1440	43.5%	525	15.9%
	2	2082	61.7%	1016	30.1%	276	8.2%
L-H125-S150	1	1725	52.4%	1223	37.1%	346	10.5%
	2	2436	69.1%	792	22.5%	296	8.4%
L-H125-S200	1	1812	53.9%	1056	31.4%	497	14.8%
	2	2740	79.1%	566	16.3%	156	4.5%
L-H80S100	1	1101	36.2%	1528	50.2%	414	13.6%
	2	2560	78.1%	488	14.9%	228	7.0%
L-H160-S100	1	1801	53.8%	1030	30.8%	518	15.5%
	2	2956	81.0%	352	9.6%	341	9.3%
L-H125-S100(U)	1	2014	61.9%	996	30.6%	243	7.5%
	2	2812	79.6%	460	13.0%	262	7.4%
L-H160-S100(D)	1	1380	40.8%	1269	37.5%	733	21.7%
	2	1387	42.4%	1263	38.6%	621	19.0%
N-H125-S100	1	1871	57.2%	1028	31.4%	373	11.4%
	2	2116	65.8%	840	26.1%	261	8.1%
R-H125-S100	1	1732	51.5%	1053	31.3%	576	17.1%
	2	2600	71.3%	772	21.2%	273	7.5%
U-H125-S100	1	1139	34.3%	1673	50.3%	512	15.4%
	2	1016	28.3%	2212	61.6%	365	10.2%

Note: The proportion is the ratio of the energy absorbed by each component to the total internal energy of the beam.

5. Summary and Conclusions

This study investigates the dynamic response of stainless steel-lightweight high ductility cement composite beam under two impacts through experimental and numerical approaches. The main conclusions based on the test and numerical investigations are as follows:

(1) The main failure modes of the composite beam under two impacts are: flexural failure with bond-slip, flexural failure, and shear failure. The specimens with large stud spacing and low height show stud fracture and separation of steel plate and concrete. The upper steel plate in the NC specimen buckles under impact, due to concrete spalling. The concrete type of the

core material has a significant influence on the degree of shear connection and shear resistance of the composite beam, thus causing different failure modes.

(2) Under two impacts, the degradation of the impact-resistance of the composite beams is mainly characterized by the decrease of the average impact force P_{ave}, the increase of the maximum displacement D_{max}, the decrease of the dynamic global stiffness k, and the decrease of the energy absorption E_w through deformation. Among them, the thickness of the core layer has the greatest influence on the reduction of P_{ave} and k, while the number of layers has considerable influence on the increase of D_{max}.

(3) Among all the parameters, the type of concrete affects the most the impact response of the composite beam under two impacts. The impact-resistance of the NC beam deteriorates severely under the second impact. The UHPC beam has a higher impact resistance under two impacts, but have lower specific energy absorption due to its higher self-weight. In contrast, composite beams with LHDCC as well as RLHDC have lower self-weight, showing better impact resistance and excellent specific energy absorption. In addition, the use of double-layer cores with the same steel ratio can reduce performance deterioration of the composite beams under two impacts. For engineering design purpose, the performance of the composite beams under two impacts can be ensured by improving the degree of shear connection (η) and increasing the number of core layers.

(4) The multi-drop hammer modeling method simplifies the numerical simulation process for modelling two impacts conditions. This study had proposed a constitutive calibration method for new material LHDCC. The CSCM constitutive parameters of LHDCC are calibrated by uniaxial and triaxial tests. The agreement between the numerical simulation results and the test results has demonstrated the predictive capability of the calibrated model. Based on the FE results, it is found that: 1) the steel plate has the largest energy dissipation capacity for specimen with flexural failure, while the concrete has the largest energy dissipation capacity for the specimens with shear failure; 2) the energy dissipated from the steel plates decreases with the increase of stud spacing and the energy dissipated from the concrete increases with the increase of concrete thickness; 3) As the number of impacts increases the energy absorbed by the concrete increases, while the energy absorbed by the steel plate decreases; 4) In the second impact, the energy absorbed by the steel plate in the single-layer specimen decreased severely. In contrast, the steel plate in the double-layer specimen remains the same energy dissipation capacity under two impacts with the same steel ratio.

Acknowledgement

The authors would like to acknowledge the research grant received from the National Natural Science Foundation of China (Grants No. 51978407), Guangdong Outstanding Youth Fund (Grants No. 2022B1515020037), Shenzhen International Science and Technology Joint Project (Grants No. GJHZ20200731095802008), Guangdong Natural Science Foundation (Grants No. 2021A1515010932), and Guangdong Provincial Key Laboratory of Durability for Marine Civil Engineering (SZU) (Grant No. 2020B1212060074).

Data Availability Statement

All data, models, and code generated or used during the study appear in the submitted article.

References

[1] Zhu L, Faulkner D. Damage estimate for plating of ships and platforms under repeated impacts[J]. Marine structures, 1996, 9(7): 697-720.

[2] Cai W, Zhu L, Qian X. Dynamic responses of steel plates under repeated ice impacts[J]. International Journal of Impact Engineering, 2022, 162: 104129.

[3] Said A M I, Mouwainea E M. Experimental investigation on reinforced concrete slabs under high-mass low velocity repeated impact loads[J].Structures, 2022, 35: 314-324.

[4] Huang Z Y, Wang J Y, Liew J Y R, et al. Lightweight steel–concrete–steel sandwich composite shell subject to punching shear[J]. Ocean Engineering, 2015, 102: 146-161.

[5] Guo Y T, Tao M X, Nie X, et al. Experimental and theoretical studies on the shear resistance of steel–concrete–steel composite structures with bidirectional steel webs[J]. Journal of Structural Engineering, 2018, 144(10): 04018172.

[6] Wang Y, Liew J Y R, Lee S C. Theoretical models for axially restrained steel-concrete-steel sandwich panels under blast loading[J]. International Journal of Impact Engineering, 2015, 76: 221-231.

[7] Liew J Y R, Sohel K M A, Koh C G. Impact tests on steel–concrete–steel sandwich beams with lightweight concrete core[J]. Engineering Structures, 2009, 31(9): 2045-2059.

[8] Sohel K M A, Liew J Y R. Behavior of steel–concrete–steel sandwich slabs subject to impact load[J]. Journal of Constructional Steel Research, 2014, 100: 163-175.

[9] Remennikov A M, Kong S Y, Uy B. The response of axially restrained non-composite steel–concrete–steel sandwich panels due to large impact loading[J]. Engineering Structures, 2013, 49: 806-818.

[10] Remennikov A M, Kong S Y. Numerical simulation and validation of impact response of axially-restrained steel–concrete–steel sandwich panels[J]. Composite Structures, 2012, 94(12): 3546-3555.

[11] Zhao W Y, Guo Q Q. Experimental study on impact and post-impact behavior of steel-concrete composite panels[J]. Thin-Walled Structures, 2018, 130: 405-413.

[12]Zhao W Y, Guo Q Q, Dou X, et al. Impact response of steel-concrete composite panels: Experiments and FE analyses[J]. Steel and Composite Structures, 2018, 26(3): 255-263.

[13] Xu S, Wu P, Liu Z, et al. Calibration of CSCM model for numerical modeling of UHPCFTWST columns against monotonic lateral loading[J]. Engineering Structures, 2021, 240: 112396.

[14] Jia P C, Wu H, Wang R, et al. Dynamic responses of reinforced ultra-high performance concrete members under low-velocity lateral impact[J]. International Journal of Impact Engineering, 2021, 150: 103818.

[15] Wu H, Ren G M, Fang Q, et al. Response of ultra-high performance cementitious composites filled steel tube (UHPCC-FST) subjected to low-velocity impact[J]. Thin-Walled Structures, 2019, 144: 106341.

[16] Huang Z Y, Zhao X L, Zhang W. Flexural Impact Performance of Stainless Steel–Lightweight Concrete Composites for Marine Structures[J]. Journal of Structural Engineering, 2022, 148(9): 04022114.

[17] Huang Z Y, Wang F, Zhou Y, et al. A novel, multifunctional, floatable, lightweight cement composite: development and properties[J]. Materials, 2018, 11(10): 2043.

[18] Huang Z Y, Sui L, Wang F, et al. Dynamic compressive behavior of a novel ultra-lightweight cement composite incorporated with rubber powder[J]. Composite Structures, 2020, 244: 112300.

[19] Baddoo N R. Stainless steel in construction: A review of research, applications, challenges and opportunities[J]. Journal of Constructional Steel Research, 2008, 64: 1199–1206.

[20] Huang Z Y, Zhao X, Zhang W, et al. Load transfer mechanism of novel double-layer steel-LHDCC-steel sandwich panels under punching loads[J]. Engineering Structures, 2021, 226: 111427.

[21] British Standards Institution. BS EN 1994-1-1. Eurocode 4: Design of composite steel and concrete structures-Part 1.1: General rules and rules for buildings. 2004, London.

[22] China Iron and Steel Association. T/CISA 022-2019. 08Cr19Mn6Ni3Cu2N High Strength Nitrogen Austenitic Stainless Steel Plate and Strip.

[23] Cai J, Ye J, Chen Q, et al. Dynamic behaviour of axially-loaded RC columns under horizontal impact loading[J]. Engineering Structures, 2018, 168: 684-697.

[24] Othman H, Marzouk H. Finite-element analysis of reinforced concrete plates subjected to repeated impact loads[J]. Journal of Structural Engineering, 2017, 143(9): 04017120.

[25] Murray Y D. Users manual for LS-DYNA concrete material model 159: No. FHWA-HRT-05-062 [R]. Colorado Springs: Federal Highway Administration, 2007: 1-74.

[26] Jiang H, Zhao J. Calibration of the continuous surface cap model for concrete[J]. Finite Elements in Analysis and Design, 2015, 97: 1-19.

[27] Chen W F. Plasticity in reinforced concrete[M]. NewYork: J. Ross Publishing, 2007: 19-47.

[28] Huang Z Y, Liew J Y R. Numerical studies of steelconcrete-steel sandwich walls with J-hook connectors subjected to axial loads[J]. Steel and Composite Structures, 2016, 21(3): 461-477.

[29] Mills L L, Zimmerman R M. Compressive strength of plain concrete under multiaxial loading Conditions[J]. ACI Journal Proceedings, 1970, 60(10): 802–807.

[30] Murray Y D, Abuodeh A Y, Bligh R P. Evaluation of LS-DYNA concrete material model 159:No. FHWA-HRT-05-063 [R]. Colorado Springs:Federal Highway Administration, 2007: 5-45.

[31] Jia S, Tan Q, Ye J, et al. Experiments on dynamic mechanical properties of austenitic stainless steel S30408 and S31608[J]. Journal of Constructional Steel Research, 2021, 179: 106556.

[32] Pham T M, Hao Y, Hao H. Sensitivity of impact behaviour of RC beams to contact stiffness[J]. International Journal of Impact Engineering, 2018, 112: 155-164.